Miscibility gap and possible intrinsic Griffiths phase in $Sr(Fe_{1-x}Mn_x)_2As_2$ crystals grown by transition metal arsenide flux

Long Chen [1,2] Cheng Cao [1,2] Hongxiang Chen,[1] Jiangang Guo [1,3] Jie Ma [4] Jiangping Hu,[1,3] and Gang Wang [1,3,5,*]

[1]*Beijing National Laboratory for Condensed Matter Physics, Institute of Physics, Chinese Academy of Sciences, Beijing 100190, China*

[2]*University of Chinese Academy of Sciences, Beijing 100049, China*

[3]*Songshan Lake Materials Laboratory, Dongguan, Guangdong 523808, China*

[4]*Key Laboratory of Artificial Structures and Quantum Control (Ministry of Education), Shenyang National Laboratory for Materials Science, School of Physics and Astronomy, Shanghai Jiao Tong University, Shanghai 200240, China*

[5]*School of Physical Sciences, University of Chinese Academy of Sciences, Beijing 100049, China*

(Received 1 March 2020; revised 13 January 2021; accepted 4 March 2021; published 9 April 2021)

The crystal structure, magnetic, electronic, and thermal properties of $Sr(Fe_{1-x}Mn_x)_2As_2$ crystals grown by transition metal arsenide flux have been systematically investigated. A miscibility gap with x ranging from 0.4362(4) to 0.9612(9) is found in the $Sr(Fe_{1-x}Mn_x)As_2$ system—for $x < 0.4362(4)$, the phase remains in the parent tetragonal structure [space group $I4/mmm$ (No. 139)], whereas for $x > 0.9612(9)$, the phase exhibits a trigonal structure [space group $P\text{-}3\,m1$ (No. 164)]. Based on our observation, the spin density wave order for $x < 0.0973(1)$ is suppressed, followed by an abnormal and broadened increase in the ordering temperature from $x = 0.0973(1)$ to $x = 0.2055(2)$. No real-space phase separation of Mn and Fe was detected for $x < 0.2055(2)$, indicating that the broadened increase in ordering temperature is attributable to a possibly intrinsic Griffiths phase. No superconducting signal was observed down to 2 K in the whole composition range with $0 < x < 1$. A phase diagram with multicritical points of Mn-doped $SrFe_2As_2$ system is established accordingly.

DOI: 10.1103/PhysRevB.103.134509

I. INTRODUCTION

The discovery of superconductivity [1] and the subsequent enhancement of superconducting (SC) transition temperature (T_c) up to 55 K in doped *RE*FeAsO (*RE* = rare earth) [2–5] have attracted great attention in the research of layered FeAs compounds over the past decade [6–8]. The $ThCr_2Si_2$-type (122-type) AFe_2As_2 (A = Eu, Sr, Ba, and Ca) compounds featuring similar FeAs layers in their structures [9–13] exhibit many similar features to those of *RE*FeAsO, e.g., both have similar densities of states near the Fermi surface [7]. The FeAs layer, serving as a carrier conduction layer [14–17], confines the conduction carriers within quasi-two dimensions and leads to strong interactions among these conduction carriers. For structure and property tuning, substituting A with alkali metals, such as K [18–20] or Na [21], in AFe_2As_2 is an effective route. Another effective route is to substitute Fe with transition metals [22]. For instance, superconductivity in AFe_2As_2 (A = Sr and Ba) can be achieved by electron doping—Co [23,24], Ni [25,26], Rh [27], or Pd [28] doping—at the Fe site, but not hole doping by Cr [29,30] or Mn [31,32]. This demonstrates the electron-hole asymmetry in high-(T_c) Fe pnictides [33]. Suppressing the spin density wave (SDW) order by doping or applying external pressure [34,35] can induce not only superconductivity with a dome-like-shape SC region but also phases with other emerging phenomena, e.g., the quantum critical point (QCP) [33,36], coexisting SC and magnetic states [21,37], or nematic phases [38].

The Mn-doped $BaFe_2As_2$ was reported as a nonsuperconductor due to its localized Mn spin moments [39,40]. Later, the lack of superconductivity was attributed to the absence of appropriate magnetic excitations as revealed by resonant inelastic x-ray scattering studies [41]. There is a large miscibility gap in $Ba(Fe_{1-x}Mn_x)_2As_2$ with $0.12 < x < 1$ when slowly cooled down to room temperature (RT) from 1273 K, and the gap narrows to $0.2 < x < 0.8$ by quenching with liquid nitrogen at 1273 K [42]. With an increase in Mn, SDW is first suppressed for $x < 0.1$, then becomes extremely broad and is no longer detectable up to $x = 0.147$ [43]. For $x > 0.1$, an evident broad minimum is observed in the derivative of the resistance, and the corresponding transition temperature increases gradually with an increase in Mn content [43]. Neutron scattering and high-resolution single-crystal x-ray diffraction (SCXRD) measurements on $Ba(Fe_{1-x}Mn_x)_2As_2$ show the missing tetragonal-to-orthorhombic structural transition, whereas the magnetic order with a propagation vector of (1/2 1/2 1) persists beyond $x = 0.102$ [31,40]. Moreover, these unique behaviors can be described by a possible Griffiths-type phase based on nuclear magnetic resonance, neutron Larmor diffraction, muon spin resonance, and inelastic neutron scattering (INS) [44].

Usually, the Griffiths region represents a two-phase region in a strongly disordered system containing a disordered paramagnetic phase and a magnetically ordered phase. The Griffiths region alters the critical scaling behavior of a phase transition by changing the power-law scaling to exponential law or completely destroys the phase transition [45–50]. The Griffiths region may result in the appearance of qualitatively new electronic or magnetic states, such as

*gangwang@iphy.ac.cn

colossal magnetoresistance [51], quantum spin glass [52,53], or (anomalous) quantum Griffiths singularity [54,55]. The INS measurement on $Ba(Fe_{1-x}Mn_x)_2As_2$ single crystals with $x = 0.075$ shows the coexistence of spin excitations of antiferromagnetic (AFM) wave vectors [$\mathbf{Q}_{AF} = \mathbf{Q}_{stripe} = (\pi, 0)$] for $BaFe_2As_2$ and [$\mathbf{Q} = \mathbf{Q}_{Neel} = (\pi, \pi)$, rotated 45° from $\mathbf{Q}_{AF}$] vectors for $BaMn_2As_2$ [40,56]. These unexpected properties were theoretically explained by the cooperative behaviors of the magnetic impurities and the conduction electrons in a real-space five-band model [57]. Because of the high Néel temperature ($T_N = 625$ K) of $BaMn_2As_2$ [58], the influence of G-type AFM order above RT cannot easily be excluded by neutron diffraction [31,40]. The similarity between the crystal structures of $BaFe_2As_2$ and $BaMn_2As_2$ poses a challenge to determine whether this is an intrinsic effect of the system or there is a real-space phase separation between Mn and Fe [56].

Contrary to the case with $BaFe_2As_2$ ($I4/mmm$) and $BaMn_2As_2$ ($I4/mmm$), the real-space phase separation between Mn and Fe in $Sr(Fe_{1-x}Mn_x)_2As_2$ can be easily determined for the quite different crystal structures of $SrFe_2As_2$ ($I4/mmm$) and $SrMn_2As_2$ (P-3 m1) [59]. In addition, the low G-type AFM ordering temperature ($T_N = 125$ K) of $SrMn_2As_2$ [59] makes it easier to recognize the G-type AFM order by neutron diffraction below RT. Thus, Mn-doped $SrFe_2As_2$ potentially provides a better platform to investigate the Griffiths-type phase. Polycrystalline $Sr(Fe_{1-x}Mn_x)_2As_2$ has been studied, and no superconductivity is induced, even for $x > 0.20$ [60]. Sn-flux-grown $Sr(Fe_{1-x}Mn_x)_2As_2$ single crystals also show no SC signal with suppressed SDW order [32]. Considering the grain boundary effects of a polycrystalline sample and the probable Sn contamination of Sn-flux-grown sample [61–63], we systematically investigate the structural, magnetic, electronic, and thermal properties of $Sr(Fe_{1-x}Mn_x)_2As_2$ crystals grown by transition metal arsenide (TMA) flux and carefully study the possible Griffiths-type phase or superconductivity. A suppressed SDW order with an ordering temperature of about 140 K at $x = 0.0973(1)$ was observed. For $0.0973(1) < x < 0.2055(2)$, the ordering temperature increases with a broadened feature, which is attributable to the possible Griffiths phase as that of $Ba(Fe_{1-x}Mn_x)_2As_2$. The real-space phase separation between Mn and Fe was observed only for $0.2055(2) < x \leqslant 0.4362(4)$, suggesting that the possible Griffiths phase for $0.0973(1) < x < 0.2055(2)$ is probably an intrinsic property of $Sr(Fe_{1-x}Mn_x)_2As_2$ system. A miscibility gap ranging from $x = 0.4362(4)$ to $x = 0.9612(9)$ was observed and no SC signal was found down to 2 K in the whole composition range with $0 < x < 1$. Finally, a global phase diagram of TMA-flux-grown $Sr(Fe_{1-x}Mn_x)_2As_2$ crystals with multicritical points was established.

II. EXPERIMENT METHODS

Mn-doped $SrFe_2As_2$ crystals were grown by a high-temperature solution method using the TMA flux. The strontium pieces (Alfa Aesar, 99%) and preheated FeAs and MnAs powder precursors were mixed using a molar ratio of $1{:}4(1-x){:}4x$ in a fritted alumina crucible set (Canfield crucible set) [64] and sealed in a fused-silica ampoule at vacuum. FeAs or MnAs precursor was prepared by heating a mixture of arsenic powder (Alfa Aesar, 99.9999+%) and ion powder (Alfa Aesar, 99.9+%) or manganese powder (Alfa Aesar, 99.95%) at 1173 or 1073 K for 10 h, respectively. The sealed ampoule was heated to 1423 K, kept for 5 h, and then slowly cooled down to 1273 K at a rate of 5 K/h. By centrifugation at 1273 K, black, shiny, and air-stable platelike crystals as large as 4 mm × 4 mm × 0.5 mm were obtained.

SCXRD patterns were collected using a Bruker D8 VENTURE diffractometer with multilayer monochromatized Mo K_α ($\lambda = 0.71073$ Å) radiation. Unit cell refinement and data merging were performed using SAINT program, and an absorption correction was applied by multiscan scanning. The solution and refinement of the crystal structure were performed using the SHELX suite [65] and JANA2006 [66]. Powder x-ray diffraction data were collected on a PANalytical X'Pert PRO diffractometer (Cu K_α radiation) operated at 40 kV voltage and 40 mA current with a graphite monochromator in a reflection mode ($2\theta = 5°$–$100°$; stepsize = 0.017°) [67]. Indexing and Rietveld refinement were performed using the DICVOL91 and FULLPROF programs [68]. Elemental analysis was conducted using a scanning electron microscope (SEM, Hitachi S-4800) equipped with an electron microprobe analyzer for semiquantitative elemental analysis in energy-dispersive spectroscopy (EDS) mode and inductively coupled plasma-atomic emission spectrometer (ICP-AES, Teledyne Leeman Laboratories Prodigy 7). For each crystal with a certain doping level, five spots in different areas were measured using EDS. The ICP-AES measurement was performed on two pieces of single crystals at each doping level. Raman-scattering measurements were performed on a HORIBA iHR550 Raman spectrometer using a laser source with a wavelength of 532 nm and power of 0.6 mW at RT. The laser beam was focused to a spot with a diameter of 1–2 μm with the X100_VIS objective. Each spectrum was collected from 50 to 500 cm^{-1} in two minutes. Temperature-dependent electronic resistance and heat capacity measurements were performed on a physical property measurement system (PPMS, Quantum Design), whereas field-dependent magnetization measurements were performed on a vibrating sample magnetometer system (VSM, Quantum Design). Contacts for standard four-probe configuration were established by attaching platinum wires using silver paint, resulting in a contact resistance smaller than 5 Ω. Samples for all measurements were cleaved along (00l) from $Sr(Fe_{1-x}Mn_x)_2As_2$ crystals using a razor blade.

III. RESULTS AND DISCUSSION

Figure 1 shows the crystal structure and chemical composition of $Sr(Fe_{1-x}Mn_x)_2As_2$ crystals. The XRD patterns of $Sr(Fe_{1-x}Mn_x)_2As_2$ crystals for $x \leqslant 0.4362(4)$ and $x \geqslant 0.9612(9)$ are shown in Figs. 1(a) and 1(b), respectively. These two series patterns can be indexed on a tetragonal structure ($I4/mmm$) and a trigonal structure (P-3m1), respectively [Fig. 1(d)]. The (00l) diffraction peaks with even l ($x \leqslant 0.4362(4)$) or integer l ($x \geqslant 0.9612(9)$) are observed, indicating that the plate surface is perpendicular to the c axis. These peaks are consistent with those of $SrFe_2As_2$ [10] and $SrMn_2As_2$ [69] polycrystalline samples, as reported. As shown by the enlarged (0010) diffraction peak, the peak

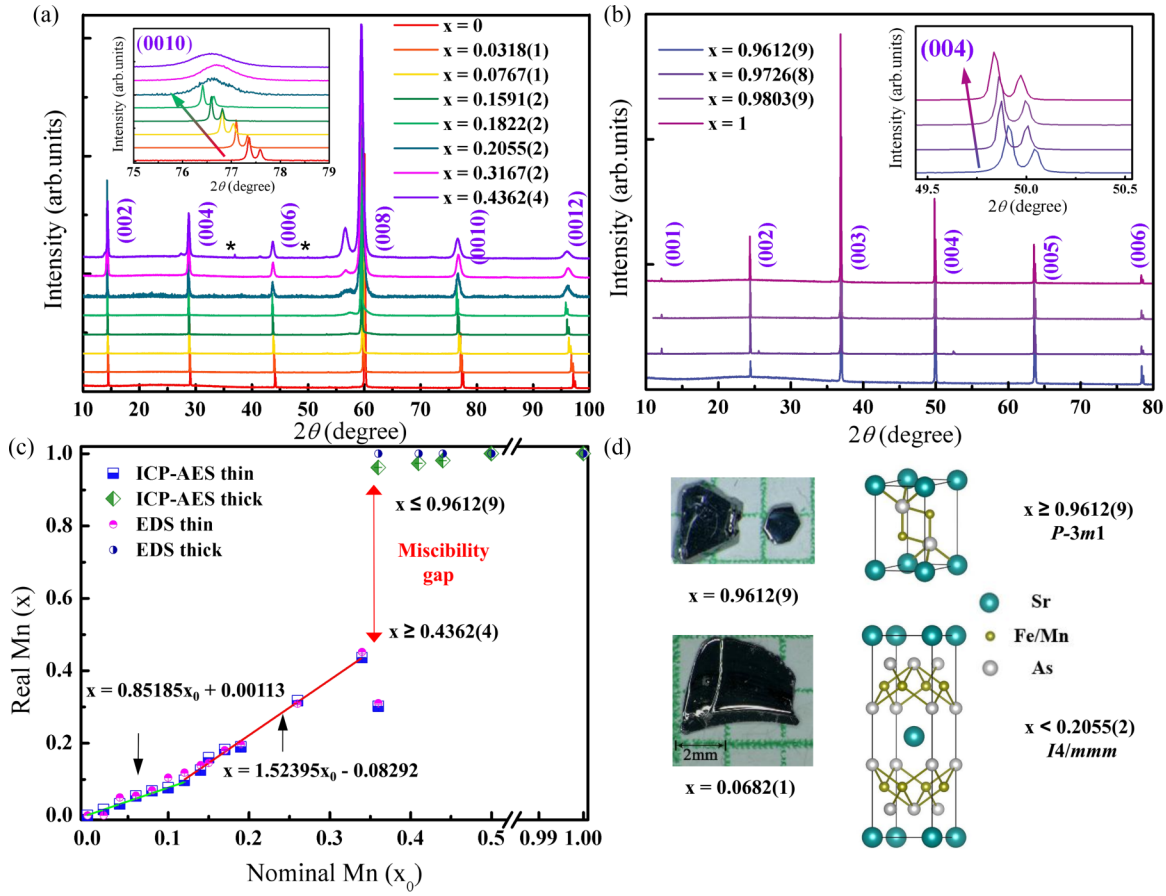

FIG. 1. (a) XRD patterns of $Sr(Fe_{1-x}Mn_x)_2As_2$ [Fe-rich side, $x \leqslant 0.4362(4)$] crystals showing $(00l)$ (l = even number) diffraction peaks. The inset is enlarged (0010) diffraction peak. The star symbols show (003) and (004) diffraction peaks of Mn-rich phase, indicating the phase separation for $x > 0.2055(2)$. (b) XRD patterns of $Sr(Fe_{1-x}Mn_x)_2As_2$ [Mn-rich phase, $x \geqslant 0.9612(9)$] crystals showing $(00l)$ (l = integer) reflections. The inset is the enlarged (004) diffraction peak. The spectra in (a) and (b) are offset for clarity. (c) Real Mn content in $Sr(Fe_{1-x}Mn_x)_2As_2$ crystals determined by ICP-AES and EDS. The lines are the linear fittings of ICP-AES results and the double arrow (red) indicates the miscibility gap. (d) Optical photographs of typical thin and thick crystals with $x = 0.0682(1)$ and $x = 0.9612(9)$ and the corresponding schematic crystal structures for $x < 0.2055(2)$ and $x \geqslant 0.9612(9)$, respectively.

position gradually shifts to a lower angle with increasing Mn content ($x < 0.2055(2)$), indicating that the lattice parameter c expands. The linearity suggests the structural homogeneity of crystals in each composition range [70]. (See Supplemental Material Fig. S1(a) for details [71]). Then, the diffraction peaks broadened at higher doping levels [$0.2055(2) \leqslant x \leqslant 0.4362(4)$] with an enlarged shoulder of (008) diffraction peak [Fig. 1(a)]. The appearance of the (003) and (004) diffraction peaks of Mn-rich $Sr(Fe_{1-x}Mn_x)_2As_2$ indicates the phase separation in the corresponding composition. At the Mn-rich side [$x \geqslant 0.9612(9)$], the (004) diffraction peak also shows a low-angle shift with increasing Mn content [inset of Figs. 1(b) and S1(b)].

Figure 1(c) and Table SI demonstrate the real Mn content of $Sr(Fe_{1-x}Mn_x)_2As_2$ crystals determined from ICP-AES and EDS. The contents of Mn (x) determined from these two techniques are consistent and have good linearity in each region. For the ICP-AES results, we found that the real Mn content (x) is lower and higher than the nominal one (x_0) before $x = 0.1254(1)$ and for $0.1591(2) \leqslant x \leqslant 0.4362(4)$, respectively. No crystals with $0.4362(4) < x < 0.9612(9)$ were obtained, indicating the existence of a large miscibility gap but smaller than that of $Ba(Fe_{1-x}Mn_x)_2As_2$ [42] (See Supplemental Material Fig. S2 for details [71]). Beyond the miscibility gap, there is a small composition range for Fe-doped $SrMn_2As_2$. Thus, we summarized the structural transition for the $Sr(Fe_{1-x}Mn_x)_2As_2$ system accordingly. With an increase in Mn content, $Sr(Fe_{1-x}Mn_x)_2As_2$ evolves from *I4/mmm* (no. 139) isostructural to $SrFe_2As_2$, to a two-phase-coexisted region, then to a miscibility gap, and finally to *P*-3*m*1 (No. 164) isostructural to $SrMn_2As_2$.

Figure 1(d) shows the optical photographs of typical thin and thick crystals with corresponding $x = 0.0682(1)$ and 0.9612(9). The thin crystal can be as large as 4 mm × 4 mm × 0.5 mm, whereas the thick crystal exhibits a hexagonal appearance. By using SCXRD, the thin crystals with $x < 0.2055(2)$ are indexed with the space group *I4/mmm* (no. 164), whereas the thick crystals with $x \geqslant 0.9612(9)$ are characterized by the *P*-3*m*1 (no. 139) space group (See Supplemental Material Table SII for details [71]). Low temperature (100 K) SCXRD data of $Sr(Fe_{1-x}Mn_x)_2As_2$ crystal with $x = 0.0973(1)$ show that there are little contractions along *a*/*b* axis (~0.23%) and *c* axis (~0.42%), indicating no phase transition from tetragonal to collapsed tetragonal phase as that of $CaFe_2As_2$

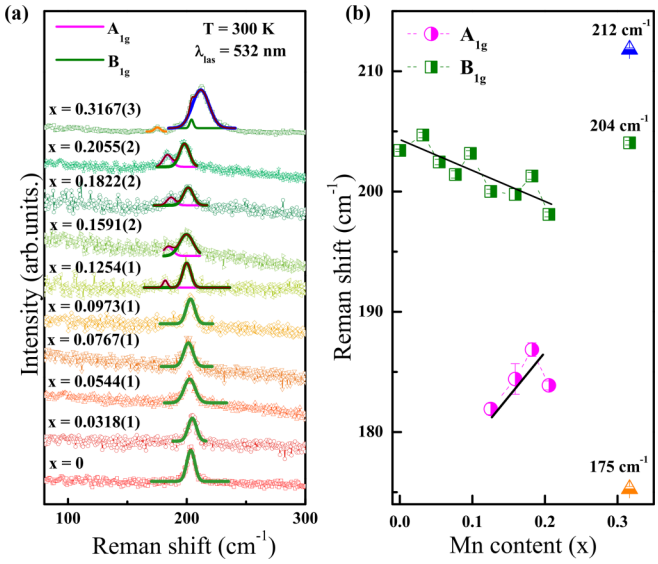

FIG. 2. (a) Raman spectra of $Sr(Fe_{1-x}Mn_x)_2As_2$ $[0 \leqslant x \leqslant 0.3167(3)]$ crystals at RT. The lines are given by Gaussian multipeak fitting. A_{1g} and B_{1g} correspond to the Raman-active modes in $SrFe_2As_2$ with characteristic peaks at 182 and 204 cm^{-1}, respectively. Each spectrum is normalized and offset for clarity. (b) Mn-content-dependent Raman modes for $Sr(Fe_{1-x}Mn_x)_2As_2$ crystals $[0 \leqslant x \leqslant 0.3167(3)]$. The two straight lines are guides to the eye.

[72–74]. The missing tetragonal-to-orthorhombic transition in $Sr(Fe_{1-x}Mn_x)_2As_2$ crystal with $x = 0.0973(1)$ is similar to that in $Ba(Fe_{1-x}Mn_x)_2As_2$ [31,40] (See Supplemental Material Table SIII for details [71]).

Figure 2(a) shows the Raman spectra of $Sr(Fe_{1-x}Mn_x)_2As_2$ crystals with $0 \leqslant x \leqslant 0.3167(3)$ at RT. For $x = 0$, the characteristic peak at 203 cm^{-1} corresponds to the B_{1g} mode of $SrFe_2As_2$, which represents the displacements of Fe atoms along the c axis [75]. For $x \leqslant 0.0973(1)$, the B_{1g} mode dominates between 80 and 300 cm^{-1}. For $Sr(Fe_{1-x}Mn_x)_2As_2$ crystals with $0.0973(1) < x \leqslant 0.2055(2)$, besides the B_{1g} mode, a new peak at 182 cm^{-1} emerges and gradually strengthens with Mn doping, which is the A_{1g} mode of $Sr(Fe_{1-x}Mn_x)_2As_2$ corresponding to the displacements of As atoms along the c axis [75]. For Mn doping higher than 0.2055(2), such as $x = 0.3167(3)$, three peaks at 175, 204, and 212 cm^{-1} are observed, among which only the peak at 204 cm^{-1} may derive from the B_{1g} mode (203 cm^{-1}). The emergence of the two new modes is attributable to the inhomogeneity in $Sr(Fe_{1-x}Mn_x)_2As_2$ crystals with $x > 0.2055(2)$. Figure 2(b) shows the Mn-content-dependent Raman modes for $Sr(Fe_{1-x}Mn_x)_2As_2$ crystals $[0 \leqslant x \leqslant 0.3167(3)]$. Both the Raman peaks corresponding to the B_{1g} mode and A_{1g} mode for $Sr(Fe_{1-x}Mn_x)_2As_2$ crystals with $0.0973(1) < x \leqslant 0.2055(2)$ are close to those of $SrFe_2As_2$ [75,76]. In this composition range, no other Raman peaks are observed, indicating the structure homogeneity.

Figure 3 demonstrates the normalized temperature-dependent dc magnetic susceptibility $(\chi/\chi_{300\,K})$ of $Sr(Fe_{1-x}Mn_x)_2As_2$ crystals measured under an applied field of 7 T parallel to the *ab* plane in the zero-field-cooling (ZFC) protocol. The magnetic transition temperatures (T_{SDW}, T^*, and T_{AFM}) are determined by maxima in $d(\chi T)/dT$ (See Supplemental Material Fig. S3(a) and S3(b) for details [71]). No hint of superconductivity is observed in the whole composition range. For $0 \leqslant x \leqslant 0.0973(1)$, the magnetic transition temperature labeled as T_{SDW} associated with the coincident SDW order and structural transition decreases from 188.6 K for $x = 0$ to 138.8 K for $x = 0.0973(1)$ [Fig. 3(a)]. For $x = 0.0973(1)$, the magnetic transition temperature becomes difficult to resolve in $\chi/\chi_{300\,K}$ curve, but it is clear in $d(\chi T)/dT$. As shown in Figs. 3(b) and S3(b), a new broadened magnetic feature with increasing transition temperature denoted as T^* emerges with increasing Mn content (x) from $x = 0.0973(1)$ to $x = 0.2055(2)$. The magnetic transition shows a broadened decreasing trend at $0.2055(2) \leqslant x \leqslant 0.4362(4)$ accompanied by phase separation [Figs. 3(c) and 1(a)]. For $x = 0.4362(4)$, there is an anomaly at 108.4 K, which can be attributed to the AFM order of Mn-rich phase due to the real-space separation of Mn and Fe. In the miscibility gap, the crystals in one batch show different magnetism (See Supplemental Material Figs. S4(a) and S4(b) for details [71]). When x is beyond the miscibility gap, the Mn-rich crystals exhibit a magnetic transition (T_{AFM}) around 110 K [Fig. 3(d)], which corresponds to the reported antiferromagnetism of $SrMn_2As_2$ [59]. The magnetic feature at low temperature may be related to FeAs impurity in the remaining flux droplet.

Figure 4 shows the normalized temperature-dependent in-plane resistance $(R_T/R_{300\,K})$ for $Sr(Fe_{1-x}Mn_x)_2As_2$ crystals. The coupled SDW ordering and structure transition temperature is determined by the minima in dR/dT. The signal of superconductivity is not observed in the whole composition range, which is consistent with the magnetization measurements. With Mn doping, the SDW ordering temperature decreases for $x \leqslant 0.0973(1)$ [Fig. 4(a)]. Meanwhile, at temperatures lower than the ordering temperature, the decreasing trend of resistance when cooling gradually shifts to an increasing one. Then, a feature with increasing characteristic temperature (T^*) emerges at x higher than 0.0973(1), and maintains up to $x = 0.2055(2)$ [Fig. 4(b)]. The value of the increasing characteristic temperature (T^*) was also determined by a minima in dR/dT [Fig. S3(d)], which is consistent with the magnetization measurements. No clear transition is observed in $R_T/R_{300\,K}$ for $0.2055(2) \leqslant x \leqslant 0.4362(4)$ [Fig. 4(c)], but a decreasing trend of the minima in dR/dT is observed [Fig. S3(d)]. The signal of the miscibility gap is also observed in the temperature-dependent resistivity (See Supplemental Material Fig. S4(c) and (d) for details [71]). At $x_0 = 0.36$, crystals with different appearances and composition growing in one batch behave differently in electronic transportation. The resistivity of thin crystals with $x = 0.3016(3)$ gradually increases with decreasing temperature, whereas the resistivity of the thick crystal with $x = 0.9612(9)$ reaches 4×10^8 Ω cm at about 170 K [Fig. 4(d)] and then goes beyond the detection limit of PPMS at lower temperature, behaving like a semiconductor. By fitting the conductivity $\sigma = 1/\rho$ with the expression $\ln(\sigma) = A - \Delta/T$ in two different temperature ranges, we obtained $\Delta = 0.77$ eV from 170 to about 210 K and $\Delta = 1.54$ eV from 210 to 300 K. The larger one is deduced to the intrinsic activation energy, and the smaller

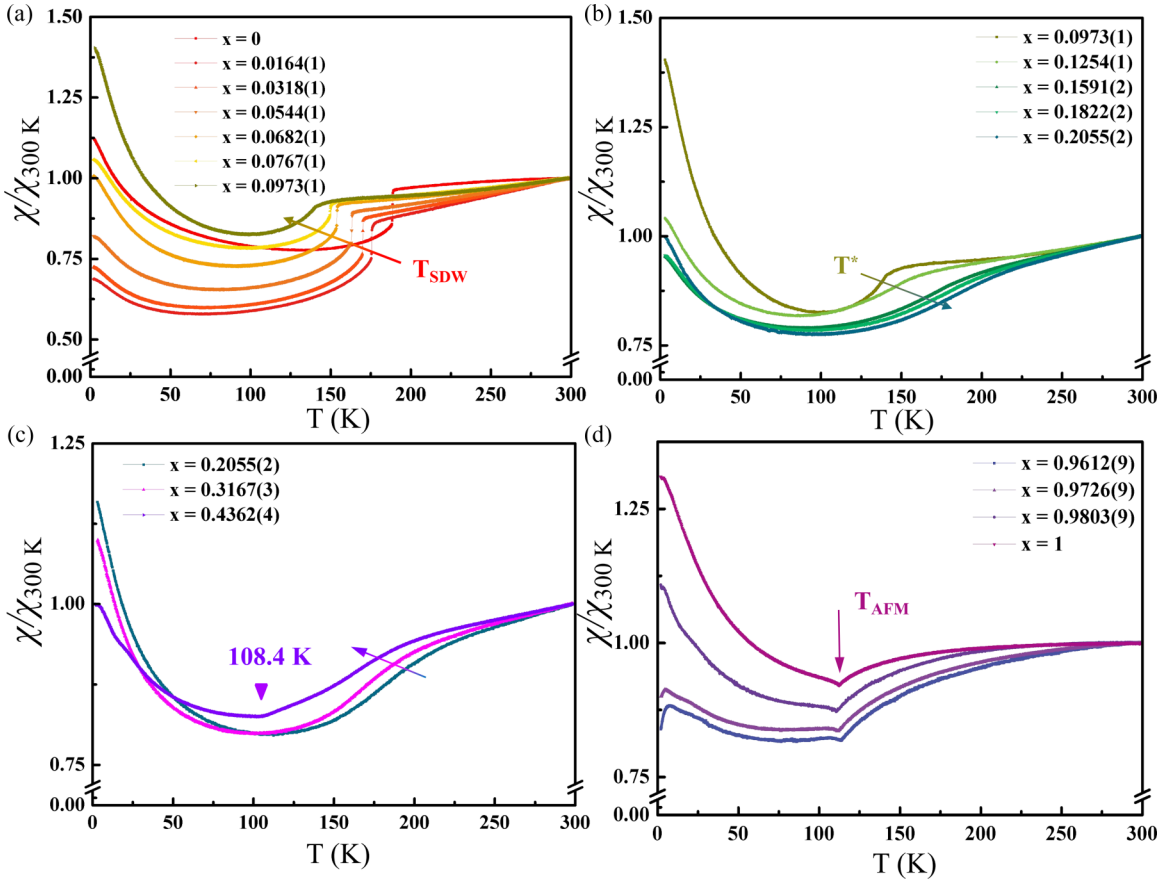

FIG. 3. Normalized temperature-dependent dc magnetic susceptibility ($\chi/\chi_{300\,K}$) of $Sr(Fe_{1-x}Mn_x)_2As_2$ crystals with an applied magnetic field of 7 T parallel to the *ab* plane in the ZFC protocol. (a) $0 \leqslant x \leqslant 0.0973(1)$. T_{SDW} denotes the suppressed SDW ordering temperature. (b) $0.0973(1) \leqslant x \leqslant 0.2055(2)$. T* denotes the unusually enhanced ordering temperature. (c) $0.2055(2) \leqslant x \leqslant 0.4362(4)$. The inverted triangle stars the kink in magnetic susceptibility for $x = 0.04362(4)$. (d) $0.9612(9) \leqslant x \leqslant 1$. T_{AFM} denotes the AFM ordering temperature for $x \geqslant 0.9612(9)$. The arrows are guides for the eyes.

one is the energy gap between the donor energy levels and conduction band or the acceptor energy levels and valence band [77,78]. Both of them have the same order of magnitude as 0.29 eV (0.64 eV) within the temperature range of 100–285 K [59] and are much larger than 85 meV fitted by the expression $\log_{10}\rho = A + 2.303\Delta/T$ between 70 and 120 K [79] for Sn-flux-grown $SrMn_2As_2$. The difference is most probably due to inevitable deviations in measurements or the flux effect as reported for $BaMn_2As_2$ [78].

Figure 5 shows the specific heat capacity of some $Sr(Fe_{1-x}Mn_x)_2As_2$ crystals with $x = 0$, 0.0767(1), 0.0973(1), and 0.2055(2). The suppression of SDW order is clearly observed for $x \leqslant 0.0973(1)$, being consistent with magnetism and resistance measurements. The single peak shows that the structural transition and SDW ordering are coupled, meanwhile the broadened and weakened tendency of the peak from $x = 0$ to $x = 0.0973(1)$ indicates the suppression of the transition. At $x = 0.2055(2)$, there is no anomaly observed, which suggests there is no structural transition and long-range magnetic order.

Based on magnetism, electronic transportation, and specific heat capacity measurements, the Mn-content-dependent critical temperature (T versus x) was summarized [Fig. 6(a)]. The linear decrease of SDW ordering temperature to about 140 K before $x = 0.0973(1)$ is consistent with the results of polycrystalline samples [60] and Sn-flux-grown crystals [32]. Then, the critical temperature shows an unusual increase with broadened feature, which has never been reported previously in this system, to the best of our knowledge. The suppression of SDW order before the critical point ($x = 0.0973(1)$) and the followed unusual increase of ordering temperature are quite similar to those in $Ba(Fe_{1-x}Mn_x)_2As_2$. For $Ba(Fe_{1-x}Mn_x)_2As_2$, the ordering temperature is suppressed from 134 to about 50 K at $x = 0.102$, followed by an enhancement to about 100 K at $x = 0.147$ [43], which has been attributed to the possible Griffiths effect [44,46,47]. For Mn-doped $BaFe_2As_2$, the enhanced ordering temperature (T*) above a critical Mn concentration, as well as other properties like the missing tetragonal-to-orthorhombic structural transition beyond the critical concentration and the unexpected G-type spin excitation (Q_{Neel}) at low concentration are successfully explained by a real-space five-band model [57] built by combining the Ruderman-Kittel-Kasuya-Yosida exchange interactions in multiorbital nested systems at the brink of an instability [80,81] with the physics of AFM Griffiths effect in itinerant systems [57,82]. In the model, the interaction between the local magnetic moment and the spin density of the itinerant electrons is denoted as $H_{imp} = J_0 \sum_{i\mu\sigma\sigma'} S_i \cdot$

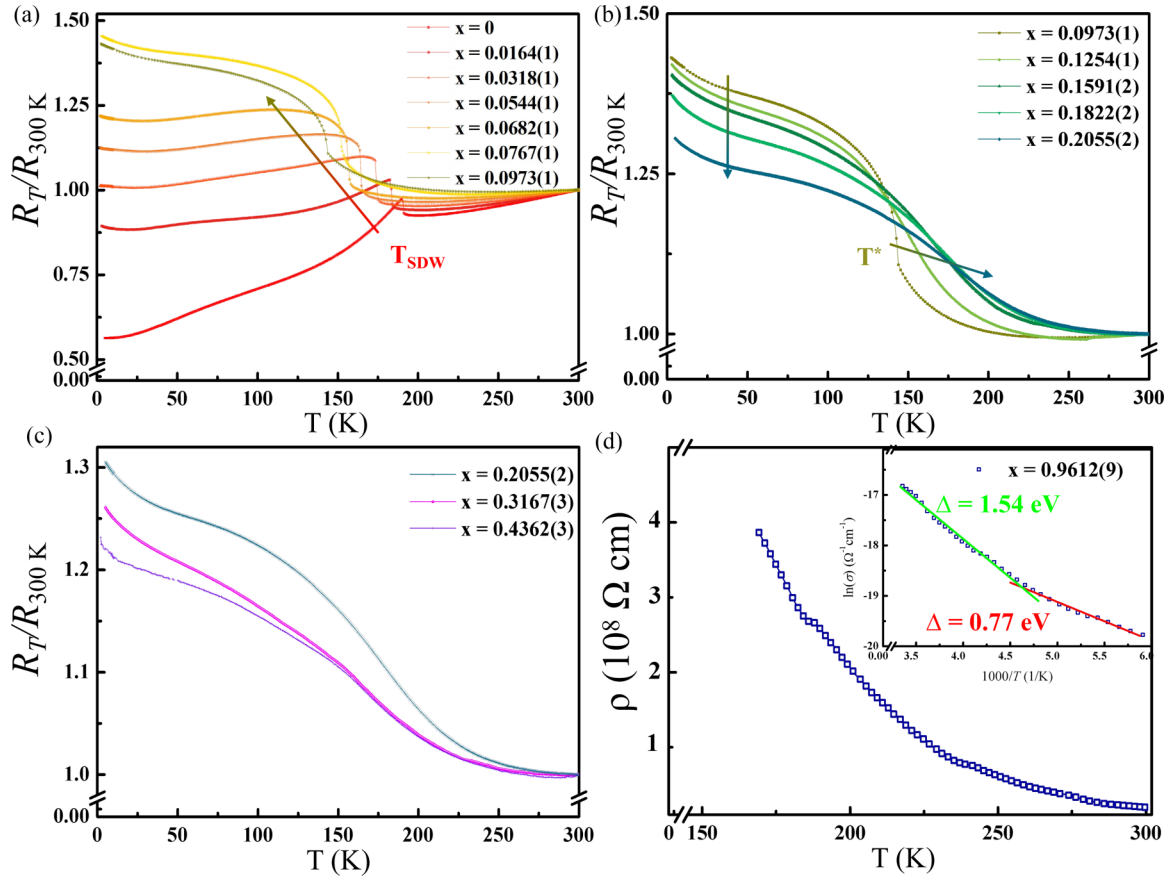

FIG. 4. Normalized temperature-dependent in-plane resistance ($R_T/R_{300\,\mathrm{K}}$) of $Sr(Fe_{1-x}Mn_x)_2As_2$ crystals. (a) $0 \leqslant x \leqslant 0.0973(1)$. T_{SDW} denotes the suppressed SDW ordering temperature. (b) $0.0973(1) \leqslant x \leqslant 0.2055(2)$. T^* denotes the unusually enhanced ordering temperature. (c) $0.2055(2) \leqslant x \leqslant 0.4362(4)$, and (d) $x = 0.9612(9)$. The inset shows $\ln(\sigma)$ versus inverse temperature $1000/T$ (where conductivity $\sigma = 1/\rho$); the solid curves represent fittings over the temperature interval by the expression $\ln(\sigma) = A - \Delta/T$, where A is a constant and Δ is the activation energy. The arrows are a guide for eyes.

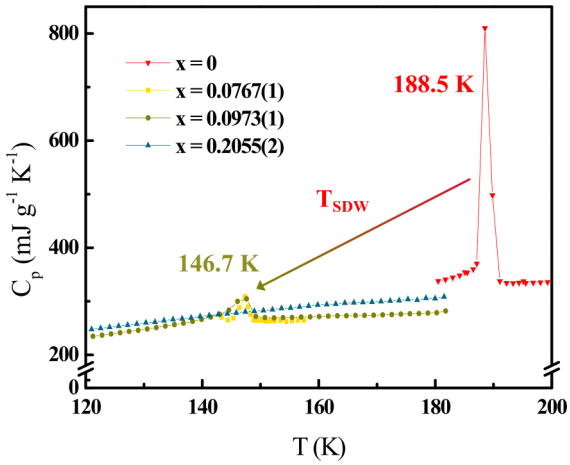

FIG. 5. Specific heat capacity of $Sr(Fe_{1-x}Mn_x)_2As_2$ crystals for $x \leqslant 0.2055(2)$. T_{SDW} denotes the suppressed SDW ordering temperature. The arrow is a guide for eyes. The difference in background may be due to the relatively high measuring temperature and mass weighing deviation.

$(c^\dagger_{i\mu\sigma}\sigma_{\sigma\sigma'}c_{i\mu\sigma'})$, where i represents the subset of lattice sites containing impurity spins (S_i), the operators $c^\dagger_{i\mu\sigma}(c_{i\mu\sigma'})$ annihilate (create) an electron at site i with spin σ in orbital state μ, the indices μ denotes the Fe $3d$ orbitals. By increasing the concentration of strong impurities ($J_0 S^z_{i\sigma} = \pm 0.8$ eV) up to 6.0%, the sharp transition is broadened and the stripe order induced by disorder can persist significantly above the ordering temperature of the clean system. Thus, the enhanced ordering temperature and the broadened tendency observed in resistivity, susceptibility, and specific heat measurements should be regarded as the signal of the possible Griffiths phase in this itinerant anti-ferromagnet. For $Sr(Fe_{1-x}Mn_x)_2As_2$, the ordering temperature is suppressed from 198 to about 140 K at $x = 0.0973(1)$, followed by a broadened enhancement to about 175 K at $x = 0.2055(2)$. The missing tetragonal-to-orthorhombic transition in $Sr(Fe_{1-x}Mn_x)_2As_2$ crystal with $x = 0.0973(1)$ is also noticed. Considering these similarities between the two systems, we would attribute such an unusual increase in ordering temperature in the $Sr(Fe_{1-x}Mn_x)_2As_2$ system to the similar Griffiths region as that of $Ba(Fe_{1-x}Mn_x)_2As_2$.

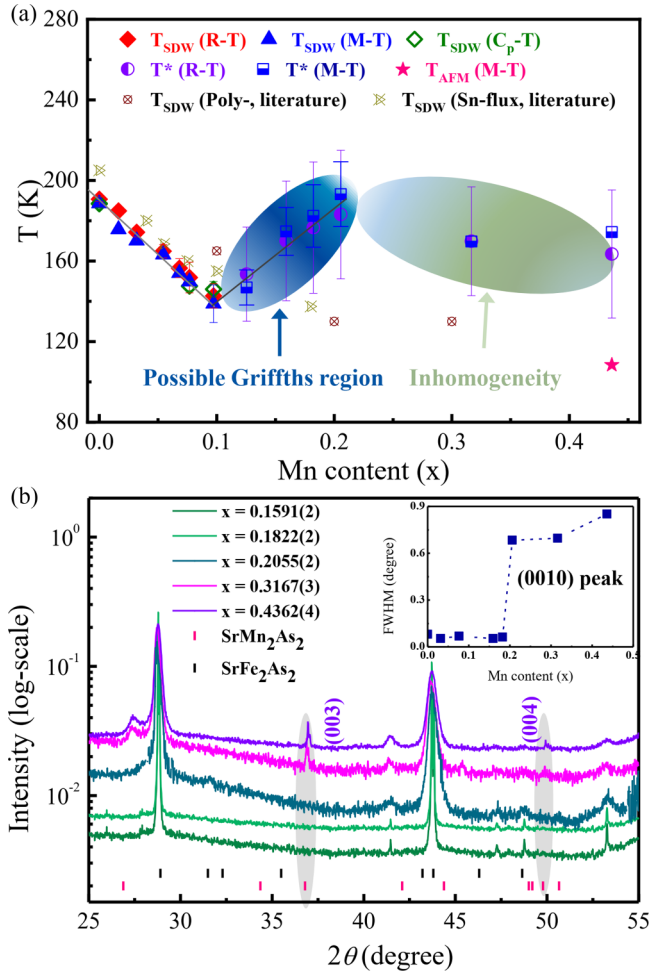

FIG. 6. (a) Mn-content-dependent critical temperature (T versus x) before the miscibility gap [$x \leqslant 0.4362(4)$]. The transition temperatures for polycrystalline $Sr(Fe_{1-x}Mn_x)_2As_2$ [T_{SDW} (Poly-, literature)] and Sn-flux-grown $Sr(Fe_{1-x}Mn_x)_2As_2$ single crystals [T_{SDW} (Sn-flux, literature)] are shown for comparison [32,60]. T_{SDW} denotes the SDW ordering temperature, T^* denotes the unusually enhanced ordering temperature beyond $x = 0.0973(1)$, and T_{AFM} denotes the AFM ordering temperature. The error bar of each ordering temperature is given by the temperature distance between points on the derivation curve ($d(\chi T)/dT$ or dR/dT) at which the curve reaches 10% of its maximum value. The solid lines represent the linear fittings of the critical temperature at different ranges of Mn content (x). Shaded areas with different colors outline the possible Griffiths region and phase-separated region for $Sr(Fe_{1-x}Mn_x)_2As_2$. (b) The log-scale XRD patterns of $Sr(Fe_{1-x}Mn_x)_2As_2$ crystals [only $0.1591(2) \leqslant x \leqslant 0.4362(4)$ for comparison]. The short vertical lines show the peak positions corresponding to $SrFe_2As_2$ and $SrMn_2As_2$ from ICSD [10,69] and the shaded areas indicate the (003) and (004) peaks for $SrMn_2As_2$. These spectra are offset for clarity. The inset shows the Mn-content-dependent FWHM of (0010) peak.

In $Ba(Fe_{1-x}Mn_x)_2As_2$, it is difficult to determine the Griffiths effect as an intrinsic effect or a real-space separation between Mn and Fe [56]. Fortunately, for $Sr(Fe_{1-x}Mn_x)_2As_2$, XRD could clearly determine the real-space separation between Mn and Fe due to the different lattice symmetry of the two parent compounds. As shown in Fig. 6(b), the XRD

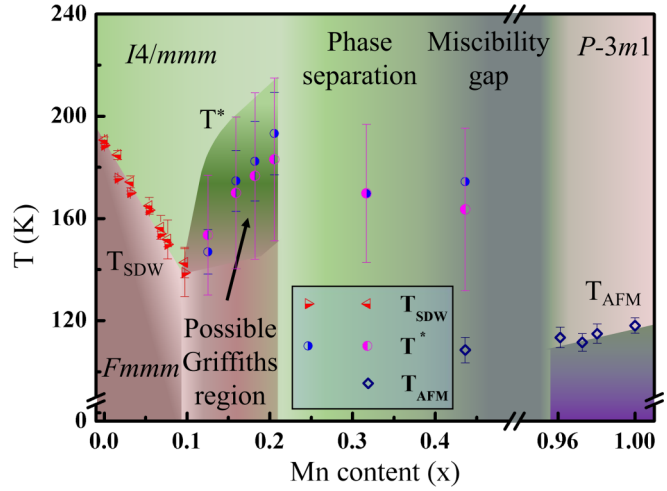

FIG. 7. Schematic phase diagram of TMA-flux-grown $Sr(Fe_{1-x}Mn_x)_2As_2$ crystals.

patterns indicate that the diffraction peaks for samples with $x = 0.1591(2)$ and $x = 0.1822(2)$ are narrow and have nearly unchanged full-width-at-half-maximum (FWHM), indicating good structure homogeneity. Moreover, the XRD patterns of samples with $0.2055(2) \leqslant x \leqslant 0.4362(4)$ present about ten times larger FWHM and the coexistence of tetragonal and trigonal phases. The narrow and stable FWHM shows good structure homogeneity for $x < 0.2055(2)$, and the coexisting phases for $0.2055 \leqslant x \leqslant 0.4362(4)$ denote structural inhomogeneity [Fig. 6(a)]. Combined with the results of Raman spectra, the unusually enhanced ordering temperature and smeared phase transition should be the intrinsic properties of $Sr(Fe_{1-x}Mn_x)_2As_2$ single crystals in the structure homogeneity region. As mentioned by Inosov *et al.* [44], in the structure homogeneity region, the Griffiths effect will enhance the ordering temperature with broadened features, whereas structural inhomogeneity would cause a decrease trend of ordering temperature. In this sense, there should be a possible intrinsic Griffiths phase in the structure homogeneity region of $Sr(Fe_{1-x}Mn_x)_2As_2$ single crystals for $0.0973(1) \leqslant x \leqslant 0.2055(2)$.

Combining the results presented above, the schematic phase diagram of TMA-flux-grown $Sr(Fe_{1-x}Mn_x)_2As_2$ crystals is established. As shown in Fig. 7, no superconductivity has been observed in the whole composition range. For $0 < x < 0.0973(1)$, $Sr(Fe_{1-x}Mn_x)_2As_2$ has a similar crystal structure and physical properties as $SrFe_2As_2$ with suppressed SDW ordering temperature. Meanwhile, the lattice parameter c expands with increasing x. For $0.0973(1) \leqslant x \leqslant 0.2055(2)$, a broadened transition feature with increasing temperature emerges. This feature could be attributed to the possible intrinsic Griffiths effect. Unlike Mn-doped $BaFe_2As_2$, the possibility of real-space separation between Mn and Fe is eliminated based on the results of XRD and Raman spectra. For $0.2055(2) < x \leqslant 0.4362(4)$, the real-space separation of Mn and Fe is observed. For $0.4362(4) < x < 0.9612(9)$, a miscibility gap does exist, and the grown crystals in one batch have different crystal structures and properties. For $0.9612(9) \leqslant x < 1$, $Sr(Fe_{1-x}Mn_x)_2As_2$ crystals have a

similar structure to that of $SrMn_2As_2$ with robust AFM order and semiconductorlike transport behavior.

More investigations, such as synchrotron diffraction, low temperature or polarized Raman-scattering, scanning tunneling microscopy/spectroscopy, or INS will be needed to further confirm the existence of the Griffiths phase. Further, it is predicted that the Griffiths effect can smear the nematic quantum phase transition in inhomogeneous systems [83], and $Sr(Fe_{1-x}Mn_x)_2As_2$ system could be a candidate to satisfy that. Compared with other transition metal-doped AFe_2As_2 (A = Eu, Sr, Ba, and Ca) systems [24–27,60,76,84–86], the behavior due to the possible Griffiths effect has only been found in Mn-doped systems [44], to the best of our knowledge. The results above will be helpful to understand the uniqueness of Mn-doped systems and reveal the origin of the Griffiths phase, or to explore more novel phases.

Beyond the AFe_2As_2 (A = Eu, Sr, Ba, and Ca) system, it is found that a tiny amount of Mn (0.2%) points toward the presence of a QCP at the crossover between SC and magnetic states in $LaFe_{1-x}Mn_xAsO_{0.89}F_{0.11}$ [36]. Mn-doped $K_{0.8}Fe_2Se_2$ will cause magnetic pairing to break and T_c to be suppressed rapidly [87,88]. By a two-step substitution in (Li, Fe)OHFeSe—first, the tetrahedral site in (Li, Fe)OH layers and then the site in the superconductivity-dominating FeSe layers—lightly Mn-substituted (Li, Fe)OHFeSe single crystals show a V-shaped change in the lattice parameter and a re-enhancement of T_c for $0.02 < x < 0.07$ [89]. For $Sr(Fe_{1-x}Mn_x)_2As_2$, there is no signal of superconductivity observed in the whole composition range, which is attributable to the non-SC parent phase $SrFe_2As_2$. High pressure may be useful to realize the QCP or superconductivity in this doped system.

IV. CONCLUSION

In summary, the crystal structure, magnetic, electronic, and thermal properties of $Sr(Fe_{1-x}Mn_x)_2As_2$ crystals grown by TMA flux have been systematically investigated. No signal of superconductivity is observed at temperatures down to 2 K. The substitution of Fe by Mn first suppresses the SDW order before a critical point at $x = 0.0973(1)$. Then, a broadened ordering temperature appears, which implies a possibly intrinsic Griffiths region without real-space separation of Mn and Fe. With higher Mn content [$x \geqslant 0.2055(2)$], the real-space separation of Mn and Fe is observed for the coexisting tetragonal and trigonal structures. In the following, a large miscibility gap from $x = 0.4362(4)$ to $x = 0.9612(9)$ as that in Mn-doped $BaFe_2As_2$ emerges. Beyond the miscibility gap, the Fe-doped $SrMn_2As_2$ exhibits a robust AFM order. Accordingly, a global phase diagram of TMA-flux-grown $Sr(Fe_{1-x}Mn_x)_2As_2$ with multicritical points is established. $Sr(Fe_{1-x}Mn_x)_2As_2$ provides a platform to investigate the origin of the Griffiths-type phase potentially and satisfy novel phases like the smeared nematic quantum phases or superconductivity.

ACKNOWLEDGMENTS

L. Chen and G. Wang acknowledge X. L. Chen of the Institute of Physics, Chinese Academy of Sciences and Q. S. Lin of the Ames Laboratory for discussions. This work was partially supported by the National Natural Science Foundation of China (Grants No. 51832010, No. 51572291, and No. U2032213), the National Key Research and Development Program of China (Grants No. 2017YFA0302902, No. 2018YFE0202600, and No. 2018YFA0704300), and the Key Research Program of Frontier Sciences, Chinese Academy of Sciences (Grant No. QYZDJ-SSW-SLH013).

[1] Y. Kamihara, T. Watanabe, M. Hirano, and H. Hosono, J. Am. Chem. Soc. **130**, 3296 (2008).
[2] G. F. Chen, Z. Li, D. Wu, G. Li, W. Z. Hu, J. Dong, P. Zheng, J. L. Luo, and N. L. Wang, Phys. Rev. Lett. **100**, 247002 (2008).
[3] X. H. Chen, T. Wu, G. Wu, R. H. Liu, H. Chen, and D. F. Fang, Nature (London) **453**, 761 (2008).
[4] Z. A. Ren, J. Yang, W. Lu, W. Yi, X. L. Shen, Z. C. Li, G. C. Che, X. L. Dong, L. L. Sun, and F. Zhou, Europhys. Lett. **82**, 57002 (2008).
[5] H. Takahashi, K. Igawa, K. Arii, Y. Kamihara, M. Hirano, and H. Hosono, Nature (London) **453**, 376 (2008).
[6] C. de La Cruz, Q. Huang, J. W. Lynn, J. Li, W. Ratcliff Ii, J. L. Zarestky, H. A. Mook, G. F. Chen, J. L. Luo, and N. L. Wang, Nature (London) **453**, 899 (2008).
[7] C. Krellner, N. Caroca-Canales, A. Jesche, H. Rosner, A. Ormeci, and C. Geibel, Phys. Rev. B **78**, 100504(R) (2008).
[8] H. H. Klauss, H. Luetkens, R. Klingeler, C. Hess, F. J. Litterst, M. Kraken, M. M. Korshunov, I. Eremin, S. L. Drechsler, R. Khasanov, A. Amato, J. Hamann-Borrero, N. Leps, A. Kondrat, G. Behr, J. Werner, and B. Buchner, Phys. Rev. Lett. **101**, 077005 (2008).
[9] M. Rotter, M. Tegel, D. Johrendt, I. Schellenberg, W. Hermes, and R. Pöttgen, Phys. Rev. B **78**, 020503(R) (2008).
[10] M. Tegel, M. Rotter, V. Weiß, F. M. Schappacher, R. Pöttgen, and D. Johrendt, J. Phys. Condens. Matter **20**, 452201 (2008).
[11] F. Ronning, T. Klimczuk, E. D. Bauer, H. Volz, and J. D. Thompson, J. Phys. Condens. Matter **20**, 322201 (2008).
[12] M. Pfisterer and G. Nagorsen, Z. Naturforsch. B **35**, 703 (1980).
[13] R. Marchand and W. Jeitschko, J. Solid State Chem. **24**, 351 (1978).
[14] Y. Kamihara, H. Hiramatsu, M. Hirano, R. Kawamura, H. Yanagi, T. Kamiya, and H. Hosono, J. Am. Chem. Soc. **128**, 10012 (2006).
[15] S. Lebegue, Phys. Rev. B **75**, 035110 (2007).
[16] T. Watanabe, H. Yanagi, T. Kamiya, Y. Kamihara, H. Hiramatsu, M. Hirano, and H. Hosono, Inorg. Chem. **46**, 7719 (2007).
[17] H. Yanagi, R. Kawamura, T. Kamiya, Y. Kamihara, M. Hirano, T. Nakamura, H. Osawa, and H. Hosono, Phys. Rev. B **77**, 224431 (2008).
[18] G. F. Chen, Z. Li, J. Dong, G. Li, W. Z. Hu, X. D. Zhang, X. H. Song, P. Zheng, N. L. Wang, and J. L. Luo, Phys. Rev. B **78**, 224512 (2008).
[19] H. Q. Yuan, J. Singleton, F. F. Balakirev, S. A. Baily, G. F. Chen, J. L. Luo, and N. L. Wang, Nature (London) **457**, 565 (2009).

[20] X. L. Wang, S. R. Ghorbani, S. I. Lee, S. X. Dou, C. T. Lin, T. H. Johansen, K. H. Müller, Z. X. Cheng, G. Peleckis, M. Shabazi, A. J. Qviller, V. V. Yurchenko, G. L. Sun, and D. L. Sun, Phys. Rev. B **82**, 024525 (2010).

[21] T. Goko, A. A. Aczel, E. Baggio-Saitovitch, S. L. Bud'ko, P. C. Canfield, J. P. Carlo, G. F. Chen, P. Dai, A. C. Hamann, W. Z. Hu, H. Kageyama, G. M. Luke, J. L. Luo, B. Nachumi, N. Ni, D. Reznik, D. R. Sanchez-Candela, A. T. Savici, K. J. Sikes, N. L. Wang, C. R. Wiebe, T. J. Williams, T. Yamamoto, W. Yu, and Y. J. Uemura, Phys. Rev. B **80**, 024508 (2009).

[22] K. Kirshenbaum, S. R. Saha, S. Ziemak, T. Drye, and J. Paglione, Phys. Rev. B **86**, 140505(R) (2012).

[23] A. S. Sefat, R. Jin, M. A. McGuire, B. C. Sales, D. J. Singh, and D. Mandrus, Phys. Rev. Lett. **101**, 117004 (2008).

[24] A. Leithe-Jasper, W. Schnelle, C. Geibel, and H. Rosner, Phys. Rev. Lett. **101**, 207004 (2008).

[25] L. J. Li, Y. K. Luo, Q. B. Wang, H. Chen, Z. Ren, Q. Tao, Y. K. Li, X. Lin, M. He, and Z. W. Zhu, New J. Phys. **11**, 025008 (2009).

[26] S. R. Saha, N. P. Butch, K. Kirshenbaum, and J. Paglione, Phys. Rev. B **79**, 224519 (2009).

[27] N. Ni, A. Thaler, A. Kracher, J. Q. Yan, S. L. Bud'ko, and P. C. Canfield, Phys. Rev. B **80**, 024511 (2009).

[28] F. Han, X. Zhu, P. Cheng, G. Mu, Y. Jia, L. Fang, Y. Wang, H. Luo, B. Zeng, B. Shen, L. Shan, C. Ren, and H. H. Wen, Phys. Rev. B **80**, 024506 (2009).

[29] S. L. Bud'ko, S. Nandi, N. Ni, A. Thaler, A. Kreyssig, A. Kracher, J. Q. Yan, A. I. Goldman, and P. C. Canfield, Phys. Rev. B **80**, 014522 (2009).

[30] A. S. Sefat, D. J. Singh, L. H. VanBebber, Y. Mozharivskyj, M. A. McGuire, R. Jin, B. C. Sales, V. Keppens, and D. Mandrus, Phys. Rev. B **79**, 224524 (2009).

[31] M. G. Kim, A. Kreyssig, A. Thaler, D. K. Pratt, W. Tian, J. L. Zarestky, M. A. Green, S. L. Bud'ko, P. C. Canfield, R. J. McQueeney, and A. I. Goldman, Phys. Rev. B **82**, 220503(R) (2010).

[32] J. S. Kim, S. Khim, H. J. Kim, M. J. Eom, J. M. Law, R. K. Kremer, J. H. Shim, and K. H. Kim, Phys. Rev. B **82**, 024510 (2010).

[33] G. Xu, H. Zhang, X. Dai, and Z. Fang, Europhys. Lett. **84**, 67015 (2009).

[34] H. Kotegawa, H. Sugawara, and H. Tou, J. Phys. Soc. Jpn **78**, 013709 (2008).

[35] P. L. Alireza, Y. C. Ko, J. Gillett, C. M. Petrone, J. M. Cole, G. G. Lonzarich, and S. E. Sebastian, J. Phys. Condens. Matter **21**, 012208 (2008).

[36] F. Hammerath, P. Bonfà, S. Sanna, G. Prando, R. De Renzi, Y. Kobayashi, M. Sato, and P. Carretta, Phys. Rev. B **89**, 134503 (2014).

[37] J. S. Kim, S. Khim, L. Yan, N. Manivannan, Y. Liu, I. Kim, G. R. Stewart, and K. H. Kim, J. Phys. Condens. Matter **21**, 102203 (2009).

[38] A. P. Dioguardi, T. Kissikov, C.-H. Lin, K. R. Shirer, M. M. Lawson, H.-J. Grafe, J.-H. Chu, I. R. Fisher, R. M. Fernandes, and N. J. Curro, Phys. Rev. Lett. **116**, 107202 (2016).

[39] Y. Texier, Y. Laplace, P. Mendels, J. T. Park, G. Friemel, D. L. Sun, D. S. Inosov, C. T. Lin, and J. Bobroff, Europhys. Lett. **99**, 17002 (2012).

[40] G. S. Tucker, D. K. Pratt, M. G. Kim, S. Ran, A. Thaler, G. E. Granroth, K. Marty, W. Tian, J. L. Zarestky, M. D. Lumsden, S. L. Bud'ko, P. C. Canfield, A. Kreyssig, A. I. Goldman, and R. J. McQueeney, Phys. Rev. B **86**, 020503(R) (2012).

[41] F. A. Garcia, O. Ivashko, D. E. McNally, L. Das, M. M. Piva, C. Adriano, P. G. Pagliuso, J. Chang, T. Schmitt, and C. Monney, Phys. Rev. B **99**, 115118 (2019).

[42] A. Pandey, V. K. Anand, and D. C. Johnston, Phys. Rev. B **84**, 014405 (2011).

[43] A. Thaler, H. Hodovanets, M. S. Torikachvili, S. Ran, A. Kracher, W. Straszheim, J. Q. Yan, E. Mun, and P. C. Canfield, Phys. Rev. B **84**, 144528 (2011).

[44] D. S. Inosov, G. Friemel, J. T. Park, A. C. Walters, Y. Texier, Y. Laplace, J. Bobroff, V. Hinkov, D. L. Sun, Y. Liu, R. Khasanov, K. Sedlak, P. Bourges, Y. Sidis, A. Ivanov, C. T. Lin, T. Keller, and B. Keimer, Phys. Rev. B **87**, 224425 (2013).

[45] I. Syozi, Prog. Theor. Phys. **34**, 189 (1965).

[46] B. M. McCoy and T. T. Wu, Phys. Rev. Lett. **21**, 549 (1968).

[47] R. B. Griffiths, Phys. Rev. Lett. **23**, 17 (1969).

[48] D. Tanaskovic, E. Miranda, and V. Dobrosavljevic, Phys. Rev. B **70**, 205108 (2004).

[49] H. v. Lohneysen, A. Rosch, M. Vojta, and P. Wolfle, Rev. Mod. Phys. **79**, 1015 (2007).

[50] T. Vojta, J. Phys. A **39**, R143 (2006).

[51] M. B. Salamon, P. Lin, and S. H. Chun, Phys. Rev. Lett. **88**, 197203 (2002).

[52] W. Wu, B. Ellman, T. F. Rosenbaum, G. Aeppli, and D. H. Reich, Phys. Rev. Lett. **67**, 2076 (1991).

[53] W. Wu, D. Bitko, T. F. Rosenbaum, and G. Aeppli, Phys. Rev. Lett. **71**, 1919 (1993).

[54] Y. Xing, H.-M. Zhang, H.-L. Fu, H. Liu, Y. Sun, J.-P. Peng, F. Wang, X. Lin, X.-C. Ma, and Q.-K. Xue, Science **350**, 542 (2015).

[55] Y. Liu, Z. Wang, P. Shan, Y. Tang, C. Liu, C. Chen, Y. Xing, Q. Wang, H. Liu, and X. Lin, Nat. Commun. **10**, 1 (2019).

[56] P. C. Dai, Rev. Mod. Phys. **87**, 855 (2015).

[57] M. N. Gastiasoro and B. M. Andersen, Phys. Rev. Lett. **113**, 067002 (2014).

[58] Y. Singh, M. A. Green, Q. Huang, A. Kreyssig, R. J. McQueeney, D. C. Johnston, and A. I. Goldman, Phys. Rev. B **80**, 100403(R) (2009).

[59] Z. W. Wang, H. X. Yang, H. F. Tian, H. L. Shi, J. B. Lu, Y. B. Qin, Z. Wang, and J. Q. Li, J. Phys. Chem. Solids **72**, 457 (2011).

[60] D. Kasinathan, A. Ormeci, K. Koch, U. Burkhardt, W. Schnelle, A. Leithe-Jasper, and H. Rosner, New J. Phys. **11**, 025023 (2009).

[61] N. Ni, S. L. Bud'ko, A. Kreyssig, S. Nandi, G. E. Rustan, A. I. Goldman, S. Gupta, J. D. Corbett, A. Kracher, and P. C. Canfield, Phys. Rev. B **78**, 014507 (2008).

[62] G. Wang, W. R. Meier, W. E. Straszheim, J. Slagle, S. L. Bud'ko, and P. C. Canfield, Phys. Rev. Mater. **2**, 104801 (2018).

[63] W. T. Jin, Y. Xiao, Z. Bukowski, Y. Su, S. Nandi, A. P. Sazonov, M. Meven, O. Zaharko, S. Demirdis, K. Nemkovski, K. Schmalzl, L. M. Tran, Z. Guguchia, E. Feng, Z. Fu, and T. Bruckel, Phys. Rev. B **94**, 184513 (2016).

[64] P. C. Canfield, T. Kong, U. S. Kaluarachchi, and N. H. Jo, Philos. Mag. **96**, 84 (2016).

[65] C. Xiao-long, L. Jing-kui, and W. Cong, Acta Phys. Sin. (Overseas Edition) **4**, 259 (1995).

[66] G. M. Sheldrick, Acta Crystallogr. A **64**, 112 (2008).

[67] V. Petříček, M. Dušek, and L. Palatinus, Z. Kristall. Cryst. Mater. **229**, 345 (2014).
[68] J. Rodríguez-Carvajal, *FullProf* (CEA/Saclay, France, 2001).
[69] E. Brechtel, G. Cordier, and H. Schäfer, Z. Naturforsch. B **33**, 820 (1978).
[70] A. R. Denton and N. W. Ashcroft, Phys. Rev. A **43**, 3161 (1991).
[71] See Supplemental Material at http://link.aps.org/supplemental/10.1103/PhysRevB.103.134509 for details concerning the structure evolution, composition and determination of ordering temperature, which includes Refs. [59,65,66,70,73].
[72] P. C. Canfield, S. L. Bud'ko, N. Ni, A. Kreyssig, A. I. Goldman, R. J. McQueeney, M. S. Torikachvili, D. N. Argyriou, G. Luke, and W. Yu, Physica C **469**, 404 (2009).
[73] S. Ran, S. L. Bud'ko, D. K. Pratt, A. Kreyssig, M. G. Kim, M. J. Kramer, D. H. Ryan, W. N. Rowan-Weetaluktuk, Y. Furukawa, B. Roy, A. I. Goldman, and P. C. Canfield, Phys. Rev. B **83**, 12, 144517 (2011).
[74] S. Ran, S. L. Bud'ko, W. E. Straszheim, J. Soh, M. G. Kim, A. Kreyssig, A. I. Goldman, and P. C. Canfield, Phys. Rev. B **85**, 16, 224528 (2012).
[75] A. P. Litvinchuk, V. G. Hadjiev, M. N. Iliev, B. Lv, A. M. Guloy, and C. W. Chu, Phys. Rev. B **78**, 060503(R) (2008).
[76] D. L. Rousseau, R. P. Bauman, and S. P. S. Porto, J. Raman Spectrosc. **10**, 253 (1981).
[77] G. L. Pearson and J. Bardeen, Phys. Rev. **75**, 865 (1949).
[78] Y. Singh, A. Ellern, and D. C. Johnston, Phys. Rev. B **79**, 094519 (2009).
[79] N. S. Sangeetha, A. Pandey, Z. A. Benson, and D. C. Johnston, Phys. Rev. B **94**, 094417 (2016).
[80] D. N. Aristov and S. V. Maleyev, Phys. Rev. B **56**, 8841 (1997).
[81] A. Akbari, I. Eremin, and P. Thalmeier, Phys. Rev. B **84**, 134513 (2011).
[82] T. Vojta, J. Low Temp. Phys. **161**, 299 (2010).
[83] T. Cui and R. M. Fernandes, Phys. Rev. B **98**, 085117 (2018).
[84] L. Zhang and D. J. Singh, Phys. Rev. B **79**, 174530 (2009).
[85] S. Saha, T. Drye, K. Kirshenbaum, N. Butch, P. Zavalij, and J. Paglione, J. Phys. Condens. Matter **22**, 072204 (2010).
[86] A. S. Sefat, K. Marty, A. D. Christianson, B. Saparov, M. A. McGuire, M. D. Lumsden, W. Tian, and B. C. Sales, Phys. Rev. B **85**, 024503 (2012).
[87] T. T. Zhou, X. L. Chen, J. G. Guo, S. F. Jin, G. Wang, X. F. Lai, T. P. Ying, H. Zhang, S. J. Shen, and S. C. Wang, J. Phys. Condens. Matter **25**, 275701 (2013).
[88] M. T. Li, L. Chen, W. L. You, J. Y. Ge, and J. C. Zhang, Appl. Phys. Lett. **105**, 192602 (2014).
[89] Y. Y. Mao, Z. A. Li, H. X. Zhou, M. W. Ma, K. Chai, S. L. Ni, S. B. Liu, J. P. Tian, Y. L. Huang, and J. Yuan, Chin. Phys. B **27**, 077405 (2018).